An Artificial Intelligence-Assisted Optimization of Imperceptible Multi-Mode Rectenna

Trung-Dung Ha, *Student Member, IEEE*, Xuecong Nie, Mobayode Akinsolu, *Senior Member, IEEE*, Bo Liu, *Senior Member, IEEE*, and Pai-Yen Chen, *Senior Member, IEEE*

Abstract— In this letter, we propose and experimentally demonstrate compact, low-profile, and optically-transparent antennas for multi-band and multi-range wireless power transfer (WPT) applications. Specifically, we put forward new types of transparent multi-band antennas that can perform the near-field reactive WPT (13.56 MHz), as well as the far-field radiative WPT (980 MHz and 2.45 GHz) within a single device. Further, such an antenna is integrated with compact, frequency-scalable rectifying circuits to form an unseeable multi-mode WPT device. We show that a hybrid inductive (13.56 MHz) and radiative (980 MHz and 2.4 GHz) WPT device can be realized with a modified inverted-F antenna (IFA) structure connected to spiral-coil virtual ground. To meet the stringent design requirements of this unobtrusive multi-band antenna, a state-of-the-art machine learning-assisted global optimization method (parallel surrogate model-assisted hybrid differential evolution for antenna optimization or PSADEA) is exploited for global optimization. We envision that the proposed transparent and flexible WPT and energy harvesting devices can be beneficial for many applications, including ubiquitous wireless charging based on smart windows and glasses, solar-radio frequency (RF) integrated power supply, wearable or textile electronics, and internet-of-things (IoTs).

Index Terms—transparent antennas, AI-assisted antenna design optimization, antenna synthesis, differential evolution, efficient global optimization, energy harvesting.

I. INTRODUCTION

THE concept of wireless power transfer (WPT) was first theorized by Nikola Tesla and his seminal experiments demonstrated that light electric bulbs can be wirelessly charged through resonant inductive coupling [1]. In general, modern WPT systems can be classified into two major categories: (1) far-field (long-range) radiative power transmission systems, known also as the rectifying antenna or rectenna technologies [2–4], and (2) near-filed (short-range) reactive power transmission systems based on the inductively coupled coils [5–7] or the capacitively coupled metallic plates [8–10]. Recently, few studies have been conducted to implement a dual-band wireless powering device that can simultaneously provide far-field and near-field WPT functions, so as to reduce the footprint and cost of devices, while enabling a wide wireless charging range [11–15]. Although these new hybrid platforms may

This manuscript is based upon work supported by the National Science Foundation under Grant No. 2210977 (EECS-CCSS program)

T. D. Ha, X. Nie, and P. Y. Chen are with the Department of Electrical and Computer Engineering, University of Illinois, Chicago, IL 60607 U.S.A.

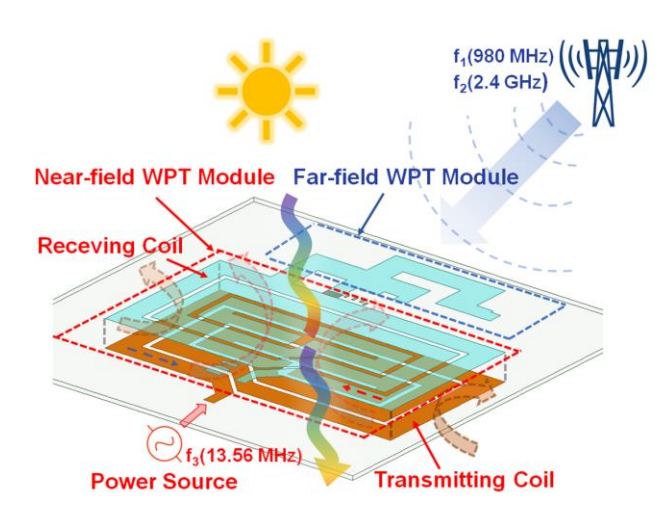


Fig. 1. Conceptual schematic illustration of the proposed hybrid optically transparent multi-band and multi-range wireless power transfer (WPT) device

leverage existing Bluetooth and NFC technologies to perform WPT within a tightly confined space, they are mostly manufactured using the traditional printed circuit board technique with rigid and opaque metal patches and microstrips, which hinders its applicability in the next-generation multifunctional transparent electromagnetic devices and systems, such as smart glasses and windows for smart cities, wearable electronics, antenna-on-display technology, and optically-transparent 5G antennas and intelligent surfaces [16–25].

In this letter, we propose a new type of multi-band and multirange WPT devices based on compact, low-profile opticallytransparent rectennas that can operate efficiently in both nearfield and far-field WPT bands to accommodate various wireless charging distances, as schematically shown in Fig. 1. This rectenna hybridizes a modified inverted-F antenna (IFA) for the radiative WPT at 980 MHz and 2.4 GHz, and a spiral coil (virtual ground plane) supporting the inductive WPT at 13.56 MHz. Since the IFA antenna has a sophisticate geometry with many design parameters and constraints, it is difficult to implement manually or through trial-and-error methods. Here, we exploit an artificial intelligence (AI)-driven design automation tool to synthesize the compact, low-profile, multi-

Corresponding author: P. Y. Chen; e-mail: pychen@uic.edu.

M. O. Akinsolu is with the Faculty of Arts, Science and Technology, Wrexham Glyndwr University, U.K.

B. Liu is with the James Watt School of Engineering, University of Glasgow, U.K.

(a) Far Field Radiative Power Transfer Module $T_X(f_1)$ Self-dual Antenna Oscillator f_1 $T_X(f_2)$ Oscillator f_2 Power amplifier

(b) Near-field Inductive Power Transfer Module

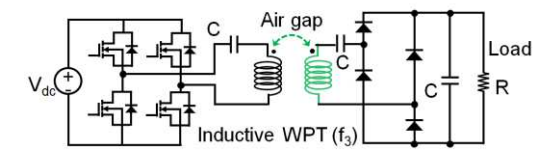


Fig. 2. Schematics of the self-dual antennas for tri-band rectenna. The antennas (highlighted by the green color) can act as a far-field WPT module (a), while its ground plane can be (b) near-field WPT module.

band inverted-F antenna with 20 design parameters. We envision that these new multi-band and multi-principle transparent antennas for WPT devices may be beneficial for a wide range of applications, including but not limited to smart windows/ glasses, integrated radio frequency solar power supply, wearable electronics, smart cities, IoT devices, and next-generation optically transparent transceivers in the 5G networks and beyond [26-29].

II. PARALLEL SURROGATE MODEL-ASSISTED HYBRID DIFFERENTIAL EVOLUTION FOR ANTENNA OPTIMIZATION

In this work, the commercial transparent conductive film (TCF), TDK Ag-Stacked film, with an optical transparency of 82% in the visible range and sheet resistance of 4 Ω /square, is used to demonstrate the proposed transparent multi-band and multi-range WPT systems. Due to the large number of design parameters and search space in optimization, the transparent antenna in Fig. 3 presents a practical design challenge, that is, it is rather difficult to have a priori knowledge of the optimum topology that provides the required frequency responses and radiation properties. Compared with the design of traditional opaque antennas based on the copper microstrip, the high surface resistance of the TCF further complicates the optimization process. To address this issue, a state-of-the-art machine learning-assisted global optimization method for antenna design was used to optimize the proposed transparent antenna. The method used is the parallel surrogate modelassisted hybrid differential evolution for antenna optimization (PSADEA) [30-31]. PSADEA belongs to the SADEA algorithm series [32-34], which is one of the state-of-the-art methods for machine learning-assisted antenna global optimization. PSADEA carries out a global search using a differential evolution (DE) driver that employs multiple complementary mutation operators adaptively. The DE-based global search is assisted by Gaussian process (GP) regression, a supervised learning technique that is used to predict antenna performances given a set of geometric parameters that define the antenna's shape. The harmonious working of DE and GP in PSADEA is achieved by employing the surrogate model-aware

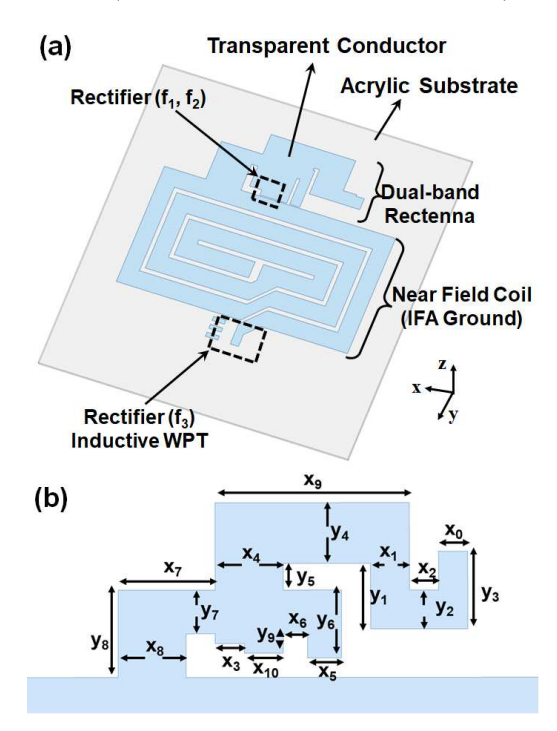


Fig. 3. (a) Geometry of the self-dual tri-band rectenna operating as inductive WPT at 13.56 MHz and radiative WPT at 980 MHz and 2.4 GHz). (b) Front view of IFA antenna with design parameters.

evolutionary search framework to allow obtaining a highly optimal design using much fewer computationally full-wave simulations. Compared to popular global optimization methods (e.g., particle swarm) for antenna design, PSADEA offers more than 20 times efficiency improvement and is suitable for addressing antenna optimization problems that traditional methods cannot solve [35-36].

The initial design of the IFA tails is presented in Fig. 3 and 20 design parameters are identified to be critical to the frequency responses. The initial topology of the IFA has a poor reflection coefficient. Our design goal is to achieve tri-band operation in different electromagnetic spectrum. Here, the AI-driven design approach was used to maximize the radiation efficiency of the transparent antenna with complicated geometry. PSADEA is performed to optimize the structure through the minimization of the cost function below:

$$F_{IFA} = w_1 \times \begin{cases} \max([-10dB - S_{11}^1, 0]) + \max([10dB + S_{11}^2, 0]) \\ + \max([-10dB - S_{11}^3, 0]) + \max([10dB + S_{11}^4, 0]) \\ + \max([-10dB - S_{11}^5, 0]) \end{cases}$$
(1)

$$+w_2 \times \left\{ \max([6dB - G_t^1, 0]) + \max([4dB - G_t^2, 0]) \right\}$$
 (1)

where S_{11}^1 , S_{11}^3 , and S_{11}^5 are the minimum in-band reflection coefficient (0.5 GHz to 0.75 GHz), (1.1 GHz to 2.25 GHz) and (2.9 GHz to 3.4 GHz), respectively, S_{11}^2 and S_{11}^4 are the maximum in-band reflection coefficient (0.95 GHz to 1 GHz), and (2.4 GHz to 2.5 GHz), respectively, G_t^1 and G_t^2 are realized gains at 0.98 GHz and 2.45 GHz, respectively, W_t and W_t the penalty coefficients set to 1 and 50, respectively. We note that W_t and W_t used respectively for the reflection coefficient term and the realized gain term can guarantee the main specification,

TABLE I
PSADEA DIMENSIONS FOR INDUCTIVE MODE ANTENNA (UNIT: MM)

Parameters	Lower Bounds	Upper Bounds	Optimum
x_0	1	10	3.9
x_I	5	20	14
x_2	1	10	6.56
x_3	5	7	6
x_4	6	25	18.6
x_5	3	6	4.9
x_6	1	18	5
x_7	20	30	20
x_8	3	17	17
<i>X9</i>	41	50	41
x_{10}	2	13	13
y_I	20	27	21.2
y_2	0	15	6.2
<i>y</i> ₃	0	16	5.5
<i>y</i> ₄	3	13	9
<i>y</i> ₅	0.5	10	1
y_6	11	25	16
y 7	5	15	6
<i>y</i> 8	13	25	13
<i>y</i> 9	1	13	12.3

TABLE II
PERFORMANCE SPECIFICATIONS FOR PROPOSED ANTENNA

Items	Specification	
Maximum Return Loss (0.95 to 1.1 GHz)	≤-10 dB	
Maximum Return Loss (2.4 to 2.5 GHz)	\leq -10 dB	
Minimum Realized Gain (0.95 to 1.1 GHz)	\geq -6 dBi	
Minimum Realized Gain (2.4 to 2.5 GHz)	≥ –4 dBi	

namely the realized gain, can be maximized, while the minor objective return loss can be achieved. When all the specifications are met, F_{IFA} becomes zero. After 964 full-wave electromagnetic simulations, PSADEA obtained the satisfactory design reported in Table II, and its reflection coefficient is as desired.

Fig. 4(a) shows the photograph of the PSADEA-optimized transparent multi-band antenna placed on the acrylic substrate with relative permittivity $\varepsilon_r = 2.6$, loss tangent $\tan(\delta) = 0.04$, and thickness t = 1.5 mm. In comparison to the initial design, the simulated reflection coefficient for PSADEA-optimized one shows a far better performance at the resonance frequencies (980 MHz and 2.45 GHz). Fig. 4(b) presents the measured reflection spectrum for the dual-band inverted-F antennas hybridized with the coil-antenna ground plane. The results show that the dual-band inverted-F antenna can resonate at 980 MHz and 2.45 GHz with bandwidths of 231 MHz and 342 MHz, respectively. The measurement and simulation results are in good agreement. In Fig. 4(c), the oscillating current is localized in the upper arm of the modified IFA structure at 980 MHz, while at 2.45 GHz the resonating current path is observed on the shorter arm, given in Fig. 4(d). Figs. 5(a) and (b) report the simulated and measured radiation patterns on the E(y-z) and H (x-z) planes for the IFA at 980 MHz and 2.45 GHz, respectively. The measured maximum realized gains are -4.5 dBi and -1.8 dBi at 980 MHz and 2.45 GHz, respectively; such values agree quite well with the simulated ones. The high

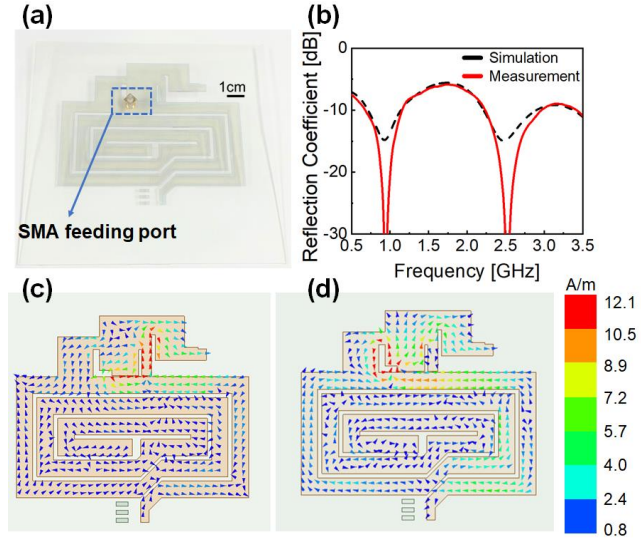


Fig. 4. (a) PSADEA-optimize hybrid rectenna for the tri-band WPT. (b) Simulated and measured reflection coefficients of the IFA antenna in (a). The surface current distribution of the optimized IFA at (c) 980 MHz and (d) 2.45 GHz.

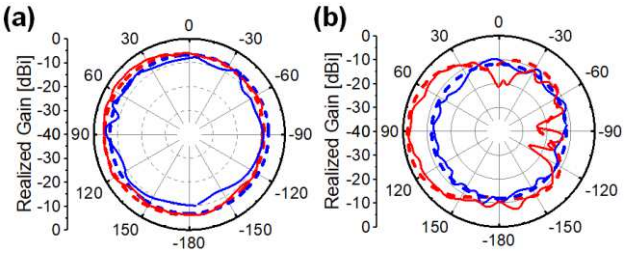


Fig. 5. Simulated (dashed lines) and measured (solid lines) radiation patterns for modified IFA at (a) 980 MHz and (b) 2.45 GHz. Here, red and blue lines represent E and H planes patterns.

conduction loss in TCF results in low radiation efficiency of 17.8% at 980 MHz and 19% at 2.45 GHz. The discrepancy between simulated and measured results is due to fabrication errors and antenna misalignment.

III. HYBRID OPTICALLY TRANSPARENT RECTENNA DESIGN

In this work, Advanced Design Simulator (ADS) has been used to design and optimize the multi-band rectifiers, consisting of bandpass filters, and matching networks built from lumped elements, and two zero-bias Schottky diodes (Skyworks SMS7630) [37] with low threshold voltage ($V_{th} = -150 \text{ mV}$) and low junction capacitance ($C_j = 0.15 \text{ pF}$), as schematically shown in Fig. 2. The values of lumped element used in Fig. 2(a) are: $C_0 = 33 \text{ pF}$, $C_1 = 22 \text{ pF}$, $C_2 = 94 \text{ pF}$ (from Wurth Elektronik), $L_1 = 11 \text{ nH}$, and $L_2 = 47 \text{ nH}$ (from TDK). By integrating the compact rectifying circuit with the fabricated IFA, a multi-band WPT device was built, and the photograph is shown in Fig. 6 (c).

Fig. 6(a) shows the PCE measurement setup for the far-field WPT; here, a horn antenna was used to transmit the radio signal from 0.5 GHz to 3.0 GHz. Fig. 7(a) reports the RF-to-DC conversion efficiencies of the multi-band rectenna at different input power levels. Here, the PCE is defined as the ratio of the output DC power to the input RF power at the antenna's input terminal, given by [4]:

$$\eta = \frac{V_L^2}{R_L P_r} \times 100 \%, \tag{2}$$

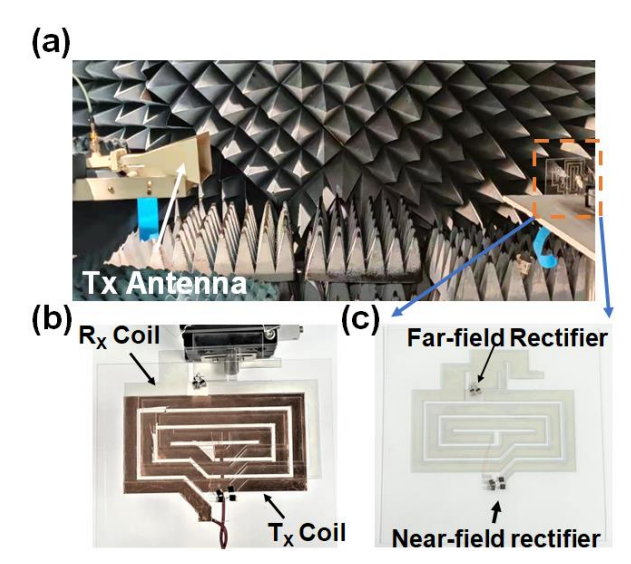


Fig. 6. Photographs of (a) the far-field radiative WPT measurement, (b) the near-field inductive WPT measurement, and (c) the fabricated multi-band and multi-range WPT device based on transparent and flexible conductive film (TDK Ag-Stacked film type B).

where V_L and R_L are respectively the output DC voltage and load resistance of the rectifying circuit, and P_r is the RF power received at the input terminal of the antenna, which can be obtained from the Friis transmission equation [38] as:

$$P_r = \frac{P_t G_t G_r}{L_{\text{eve}}} \left(\frac{\lambda_0}{4\pi R} \right)^2 \tag{3}$$

where G_t is the realized gain of the transmitting horn antenna (here; $G_t \approx 12$ dBi and 16.75 dBi at 980 MHz and 2.45 GHz, respectively), G_r is the realized gain of the receiving antenna, R is the distance between transmitter and the rectenna under test, P_t is the total transmitted power. We note that all measurements were performed in an anechoic chamber and that insertion losses in cables and connectors were excluded when determining P_t and P_r (i.e., $L_{sys} = 1$). In our PCE calculation, the maximum effective aperture of the antenna, $\sigma = (\lambda_0^2/4\pi) \times$ D_r , is used such that the finite radiation efficiency of the antenna is considered. From Fig. 7(b), we find that at the operating frequencies, the conversion efficiencies are proportional to the input power. The efficiency curves exhibit peaks at 980 MHz and 2.45 GHz for different illuminating power densities, demonstrating good dual-band matching and the potential of multi-band WPT. Fig. 7(a) reports the measured PCE as a function of RF illuminating power density at 980 MHz and 2.45 GHz; here, the illuminating power density $W_{inc} = P_t G_t / (4\pi R)^2 \times (1/L_{sys})$. Fig. 7(b) shows that the highest PCE reaches up to 55.45% at 980 MHz and 51.44% at 2.45 GHz under the delivered power density of 136.46 mW/m². Moreover, even at a relatively low RF power density of 4.41 mW/m², the measured PCE can still reach 21.81 % at 980 MHz and 20.49 % at 2.45 GHz. We note that the far-field WPT performance was characterized in the presence of the secondary coil shown in Fig. 6(b).

Next, we study the power transmission efficiency and the maximum output power level of the inductive coil used for the near-field WPT. The measurement setup is shown in Fig. 6(b), where a copper coil is used as the power transmitter. The inductive WPT at 13.56 MHz features a standard series resonate

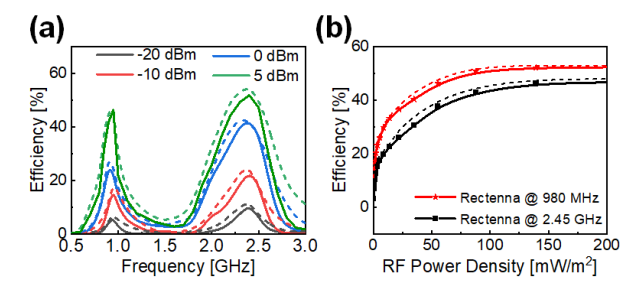


Fig. 7. (a) Frequency and (b) power dependencies of the RF-to-DC conversion efficiency for the dual-band far-field WPT module

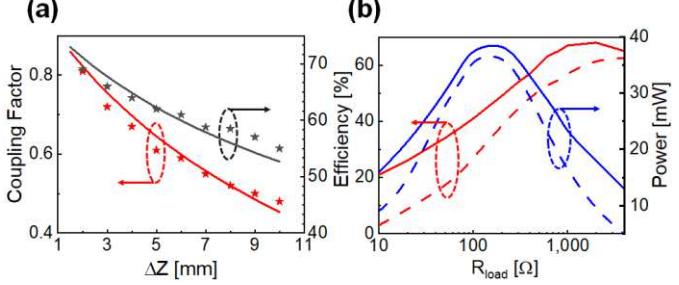


Fig. 8. (a) Inductive coupling factor and efficiency versus ΔZ for the embedded spiral coil. (b) AC-to-DC efficiency versus load resistance for the near-field inductive WPT module in Fig. 6(b-c). Measured results are represented by symbols in (a) and dashed lines in (b). Simulated results are represented by solid lines in (a) and (b).

LC tank [see Fig. 2(b)], and an adjustable capacitor (from Murata) for tuning the resonance frequency. The power source is based on a full-bridge D-class amplifier from Rigol. The fullbridge rectifier configuration comprises four Skyworks SMS7630 Schottky diodes [see Fig. 2(b)]. Fig. 8(a) reports the extracted coupling factor between the copper coil transmitter and the transparent coil receiver at different interrogation distances. As can be observed in Fig. 8(a), the coupling coefficient decreases with increasing the air gap, and a satisfactory inductive coupling strength of 0.45 and efficiency of 50% can still be obtained at a transfer distance of 10 mm. Given a typical transfer distance (5 mm) that corresponds to the magnetic coupling factor of 0.61, the efficiency and output power of this inductive WPT system are reported in Fig. 8(b). By tuning the load on the rectifier side, the maximum system efficiency of 62.8 % can be obtained with a 4 k Ω load. The maximum power transfer of 36.8 mW can be obtained at a 150 Ω load.

IV. CONCLUSION

We have proposed and experimentally demonstrated compact, low-profile, optically transparent, and flexible antenna designs that target multi-band and multi-range wireless power transmission applications. A self-dual antenna structure has been designed and optimized using a machine learning-assisted global optimization method for antenna design, PSADEA (i.e., the stripline-based radiative-inductive hybrid rectenna). The miniature transparent antennas loaded with lightweight lumped rectifier can simultaneously achieve the long-range radiative WPT and the short-range inductive WPT within a single device. Our experimental results show that the satisfactory antenna gain, impedance matching, and RF-to-DC conversion efficiency can be achieved at different operating frequencies spanning the HF and UHF bands.

REFERENCES

- T. Campi, S. Cruciani, F. Palandrani, V. De Santis, A. Hirata, and M. Feliziani, "Wireless power transfer charging system for AIMDs and pacemakers," *IEEE Trans. Microw. Theory Tech.*, vol. 64, no. 2, pp. 633–642, 2016.
- [2] X. Gu, S. Hemour, and K. Wu, "Far-Field Wireless Power Harvesting: Nonlinear Modeling, Rectenna Design, and Emerging Applications," Proceedings of the IEEE, 2021.
- [3] T. D. Ha, L. Zhu, and P.-Y. Chen, "A low-cost wide-angle multi-beam coverage Bruce rectennas for energy harvesting applications," in *IEEE AP-S/URSI*, Denver, Colorado, USA, 2021, pp. 2004–2005.
- [4] S. Ladan, A. B. Guntupalli, and K. Wu, "A high-efficiency 24 GHz rectenna development towards millimeter-wave energy harvesting and wireless power transmission," *IEEE Trans. Circuits Syst. I Regul. Pap.*, vol. 61, no. 12, pp. 3358–3366, 2014.
- [5] P.-Y. Chen and R. El-Ganainy, "Exceptional points enhance wireless readout," *Nat. Electron.*, vol. 2, no. 8, pp. 323–324, 2019.
- [6] M. Sakhdari, M. Hajizadegan, Q. Zhong, D. Christodoulides, R. El-Ganainy, and P.-Y. Chen, "Experimental Observation of P T Symmetry Breaking near Divergent Exceptional Points," *Phys. Rev. Lett.*, vol. 123, no. 19, p. 193901, 2019.
- [7] P.-Y. Chen et al., "Generalized parity-time symmetry condition for enhanced sensor telemetry," Nat. Electron., vol. 1, no. 5, pp. 297–304, 2018
- [8] F. Lu, H. Zhang, H. Hofmann, and C. Mi, "A double-sided LCLC-compensated capacitive power transfer system for electric vehicle charging," *IEEE Trans. Power Electron.*, vol. 30, no. 11, pp. 6011–6014, 2015.
- [9] F. Lu, H. Zhang, and C. Mi, "A review on the recent development of capacitive wireless power transfer technology," *Energies*, vol. 10, no. 11, p. 1752, 2017.
- [10] B. Luo, T. Long, L. Guo, R. Dai, R. Mai, and Z. He, "Analysis and design of inductive and capacitive hybrid wireless power transfer system for railway application," *IEEE Trans. Ind. Appl.*, vol. 56, no. 3, pp. 3034– 3042, 2020.
- [11] Y. Tanabe, T. Chang, A. J. Yeh, and A. S. Poon, "A small dual-band asymmetric dipole antenna for 13.56 MHz power and 2.45 GHz data transmission," *IEEE Antennas Wirel. Propag. Lett.*, vol. 13, pp. 1120– 1123, 2014.
- [12] J. Hu, W. Zhang, Y. Li, and Z. Zhang, "Compact Co-polarized PIFAs for Full-Duplex Application Based on CM/DM Cancellation Theory," *IEEE Trans. Antennas Propag.*, vol. 69, no. 11, pp. 7103–7110, 2021.
- [13] W. Lin and R. W. Ziolkowski, "Electrically small Huygens CP rectenna with a driven loop element maximizes its wireless power transfer efficiency," *IEEE Trans. Antennas Propag.*, vol. 68, no. 1, pp. 540–545, 2019.
- [14] E. Vandelle, G. Ardila, S. Hemour, K. Wu, and T. Vuong, "Compact dual-band rectenna on a new paper substrate based on air-filled technology," in *Wirel. Power Transf. Conf.*, 2019, pp. 307–311.
- [15] M. Wagih, A. Komolafe, A. S. Weddell and S. Beeby, "Broadband Compact Substrate-Independent Textile Wearable Antenna for Simultaneous Near- and Far-Field Wireless Power Transmission," in IEEE Open Journal of Antennas and Propagation, vol. 3, pp. 398-411, 2022.
- [16] M. Stoppa and A. Chiolerio, "Wearable electronics and smart textiles: A critical review," Sens., vol. 14, no. 7, pp. 11957–11992, 2014.
- [17] Y. Gao et al., "Nanoceramic VO2 thermochromic smart glass: A review on progress in solution processing," Nano Energy, vol. 1, no. 2, pp. 221– 246, 2012.
- [18] J. Park, S. Y. Lee, J. Kim, D. Park, W. Choi, and W. Hong, "An optically invisible antenna-on-display concept for millimeter-wave 5G cellular devices," *IEEE Trans. Antennas Propag.*, vol. 67, no. 5, pp. 2942–2952, 2019.
- [19] W. Lin and R. W. Ziolkowski, "Electrically small, single-substrate huygens dipole rectenna for ultracompact wireless power transfer applications," *IEEE Trans. Antennas Propag.*, vol. 69, no. 2, pp. 1130– 1134, 2020.
- [20] Y. Xu et al., "Pencil-paper on-skin electronics," in Proc. Nat. Acad. Sci. U.S.A, vol. 117, no. 31, pp. 18292–18301, 2020.
- [21] L. Zhu, T. D. Ha, Y.-H. Chen, H. Huang, and P.-Y. Chen, "A passive smart face mask for wireless cough monitoring: a harmonic detection scheme with clutter rejection," *IEEE Trans. Biomed. Circuits Syst.*, 2022.

- [22] W. Lin and R. W. Ziolkowski, "A circularly polarized wireless power transfer system for internet-of-things (IoT) applications," in Wirel. Power Transf. Conf., 2020, pp. 1–2.
- [23] Z. Ye *et al.*, "A Breathable, Reusable, and Zero-Power Smart Face Mask for Wireless Cough and Mask-Wearing Monitoring," *ACS nano*, 2022.
- [24] L. Zhu, X. Nie, P. -Y. Chen and L. J. Guo, "Transparent and Flexible Self-Dual Antennas for Hybrid Inductive/Capacitive and Radiative Power Transfer," in *Wirel. Power Transf. Conf.*, 2021, pp. 1-4.
- [25] T. D. Ha, L. Zhu, N. Alsaab, P.-Y. Chen, and J. L. Guo, "Optically transparent metasurface radome for RCS reduction and gain enhancement of multifunctional antennas," IEEE Trans. Antennas Propag., vol. 71, no. 1, pp. 67–77, Jan. 2023.
- [26] Y. Zhang, S. Shen, C. Y. Chiu and R. Murch, "Hybrid RF-Solar Energy Harvesting Systems Utilizing Transparent Multiport Micromeshed Antennas," in *IEEE Trans. Microw. Theory Techn.*, vol. 67, no. 11, pp. 4534-4546, Nov. 2019.
- [27] P. Zhang, X. Zhang and L. Li, "An Optically Transparent Metantenna for RF Wireless Energy Harvesting," in *IEEE Trans. Antennas Propag.*, vol. 70, no. 4, pp. 2550-2560, April 2022.
- [28] T. Peter, T. A. Rahman, S. W. Cheung, R. Nilavalan, H. F. Abutarboush and A. Vilches, "A Novel Transparent UWB Antenna for Photovoltaic Solar Panel Integration and RF Energy Harvesting," in *IEEE Trans.* Antennas Propag., vol. 62, no. 4, pp. 1844-1853, April 2014.
- [29] B. -Y. Yu et al., "Flexible and Wearable Hybrid RF and Solar Energy Harvesting System," in *IEEE Trans. Antennas Propag.*, vol. 70, no. 3, pp. 2223-2233, March 2022.
- [30] B. Liu, M. O. Akinsolu, N. Ali, and R. Abd-Alhameed, "A parallel surrogate model assisted evolutionary algorithm for electromagnetic design optimization A parallel surrogate model assisted evolutionary algorithm for electromagnetic design optimization," *IET Microw. Antennas Propag.*, vol. 13, no. 2, pp. 149–155, 2019.
- [31] M. O. Akinsolu, B. Liu, V. Grout, P. I. Lazaridis, M. E. Mognaschi, and P. Di Barba, "A parallel surrogate model assisted evolutionary algorithm for electromagnetic design optimization," *IEEE Trans. Emerg. Top. Comput. Intell.*, vol. 3, no. 2, pp. 93–105, 2019.
- [32] B. Liu, H. Aliakbarian, Z. Ma, G. A. Vandenbosch, G. Gielen, and P. Excell, "An efficient method for antenna design optimization based on evolutionary computation and machine learning techniques," *IEEE Trans. Antennas Propag.*, vol. 62, no. 1, pp. 7–18, 2013.
- [33] B. Liu et al., "An efficient method for complex antenna design based on a self adaptive surrogate model-assisted optimization technique," *IEEE Trans. Antennas Propag.*, vol. 69, no. 4, pp. 2302–2315, 2021.
- [34] B. Liu, S. Koziel, and N. Ali, "SADEA-II: A generalized method for efficient global optimization of antenna design," *J. Comput. Des. Eng.*, vol. 4, no. 2, pp. 86–97, 2017.
- [35] B. Liu, Q. Zhang, and G. G. Gielen, "A Gaussian process surrogate model assisted evolutionary algorithm for medium scale expensive optimization problems," *IEEE Transactions on Evolutionary Computation*, vol. 18, no. 2, pp. 180–192, 2013.
- [36] J. Zhang, M. O. Akinsolu, B. Liu, and G. A. Vandenbosch, "Automatic AI-driven design of mutual coupling reducing topologies for frequency reconfigurable antenna arrays," *IEEE Trans. Evol. Comput.*, vol. 69, no. 3, pp. 1831–1836, 2020.
- [37] https://www.skyworksinc.com/Products/Diodes/SMS7630-Series
- [38] A. Balanis, Antenna Theory: Analysis and Design 4th ed. Hoboken, NJ, USA: Wiley, 2016, pp.88-90.